Numerical simulations of multi-phase electro-hydrodynamics flows using a simple incompressible smoothed particle hydrodynamics method

F. Almasi, M.S. Shadloo, A. Hadjadj, M. Ozbulut, N. Tofighi, M. Yildiz

Numerical simulations of multi-phase electro-hydrodynamics flows using a simple incompressible smoothed particle hydrodynamics method

F. Almasi[1], M. S. Shadloo[1,2,*], A. Hadjadj[1], M. Ozbulut[3], N. Tofighi[4], M. Yildiz[4,5,6]

[1] *CORIA - UMR 6614, Normandie University, CNRS - INSA of Rouen, 76000 Rouen, France*
[2] *Institute of Chemical Process Engineering, University of Stuttgart, Stuttgart, 70199, Germany*
[3] *Engineering Faculty, Piri Reis University, 34940 Istanbul, Turkey*
[4] *Sabanci University, Faculty of Engineering and Natural Sciences,Tuzla, 34956, Istanbul, Turkey*
[5] *Integrated Manufacturing Technologies Research and Application Center, Sabanci University, Tuzla, 34956, Istanbul, Turkey*
[6] *Composite Technologies Center of Excellence, Sabanci University-Kordsa, Istanbul TechnologyDevelopment Zone, Sanayi Mah. Teknopark Blvd. No: 1/1B, Pendik, 34906, Istanbul, Turkey*

Abstract

Practically, every processing technology deals with complex multi-phase flows and predicting the fluid flow behaviour is crucial for these processes. Current study discusses the application of a mesh-less numerical methodology, i.e. Incompressible Smoothed Particle Hydrodynamics (ISPH) to investigate the behaviour of different multi-phase flow systems. This works is presented in a coherent way with increasing test problem difficulties and their concerned physical complexities. A wide range of problems including Laplace's law, bubble rising, bubble suspension under an external electric field are considered for a code validation purpose, while the numerical results manifest very good accordance with the experimental and theoretical data. Finally, we show the effectiveness of using an external electric field for controlling a complex problem such as Couette flow for a range of electrical permittivity and electrical conductivity ratios. It is noted that the Electrohydrodynamics (EHD) effect on a suspended droplet in Couette flow case is simulated for the first time using the SPH method.

Keywords: Smoothed Particle Hydrodynamics (SPH), Meshless methods, ElectroHydrodynamics (EHD), Multi-phase flow, Couette flow

1. Introduction

Predicting the behaviour of multi-phase flow systems has attracted for decades the attention of many industries due to their wide ranges of applications in the chemical engineering, aerospace engineering and renewable energy sectors, among others [1, 2, 3]. In multi-phase systems two or more fluids share interfaces which can deform/ migrate as outcome of exerted forces and constitutional laws. Some applications of multi-phase systems include boiling, condensation, water purification and petroleum refinement processes where these phenomena have been investigated mostly experimentally and theoretically. However, with the ever-increasing power of Computational Fluid Dynamics (CFD) methods, numerical simulations of these systems became of great interest among researchers [4, 5, 6].

Smoothed Particle Hydrodynamics (SPH) is a relatively recent and promising mesh-less Lagrangian method which discretizes the domain into a set of nodes, known as material particles. These particles can freely move inside the computational domain subject to an external force or particle-particle interactions. Initially introduced by Gingold and Monaghan [7], and Lucy [8] for astrophysics applications, SPH was soon found to be suitable for fluid dynamics problems, where complex geometries [9, 10, 11], large deformations [12, 13, 14], multi-phase [15, 16, 17] and multi-physics problems [18, 19, 20] are involved. A recent overview for the application of SPH can be found in [21].

One of the most important engineering problems which involves many of above cases is the Electrohydrodynamics (EHD) one, where hydrodynamics of a fluid system is coupled with its response to an external electric field. In EHD problems, one may control the interface between the two fluids (here, the droplet and the bulk fluid) by controlling the flow conditions and fluid properties [22, 23]. In such problems, the coupling may lead to a large interfacial deformation (i.e. merge/breakup) or migration. Indeed, EHD is a very complex problem including multi-phase, multi-physics and multi-scale phenomena with strong topological changes of the interface shape [24, 25]. Although, there are many experimental and theoretical studies available in the literature on the coupled modeling of EHD problems [26, 27, 28]. Nevertheless, some discrepancies between experiments and analytical data still exist [28]. As such, numerical simulations have been developed to tackle these difficulties and provide insight into EHD problems.

Considering the numerical simulations of EHD using SPH method, Shadloo et al. [29] were the first group to provide a model for such problems. They validated their code with the simple EHD deformation of droplets suspended in a neutrally buoyant Newtonian fluid. Rahmat et al. have proposed a multi phase ISPH method based on the lubrication theory and the drainage model to simulate droplet electro-coalescence for wide ranges of simulation conditions. [30, 31]. Rahmat et al. [32] also provided the first simulation results for the Rayleigh-Taylor instability under the combined effect of electric field and gravitational forces. Yet, step-by-step validation of the SPH method for each individual force using the same methodology is not well-documented. Additionally, numerical simulation of a multi-phase flow under the effects of an electric field using various scenarios ranging from low to high deformations, droplet migration, and effect of shear flow on the droplet's deformation would provide a broader perspective into the capabilities of the SPH method for such applications. To this end, this article aims at introducing a mesh-less numerical methodology, i.e. Incompressible SPH (ISPH) approach, to deal with such complex problems. Additionally, we verify the applicability of some of the used algorithms for a range of problems including hydrodynamic, capillary, gravity, shear and EHD forces.

This article is organized as follows: First, we introduce the mathematical formulation of the SPH method as well as the numerical discretization scheme.Then, we incorporate the governing equations of the multi-phase system including the conservation equations for mass, momentum and electrical charges in a Lagrangian form. Thereafter, a code validation and numerical convergence study is asserted in the absence of electric field. Numerical results cover solutions with and without electric filed sections. Additionally, the effect of surface tension through Laplace law, the effect of gravitational force, and the Couette flow for a multi-phase system are examined and validated against analytical solution and available numerical data in the literature. Finally, conclusions are provided in the last section.

2. Mathematical Formulation of SPH

The idea of SPH comes from the fact that any field variable $f(x)$ can be calculated by an exact mathematical relation as

$$f(x) = \int_{\Omega} f(x')\delta(x')dx'. \tag{1}$$

Upon approximating $\delta(x')$ by an interpolation function $W(x - x', h)$, this equation can be formulated as

$$f(x) = \int_{\Omega} f(x')W(x - x', h)dx', \tag{2}$$

where x and x' are the position vectors and h is the smoothing length. In our case, $h = \zeta dx$ where ζ=1.6 is a constant value, and dx is the initial particle spacing. The interpolation function, also known as smoothing function or kernel function, should have, among others, the following properties [33]

– Normalized over the domain

$$\int_{\Omega} W(x - x', h)dx = 1. \tag{3}$$

– Produces δ function for a small enough smoothing length

$$\lim_{h \to 0} W(x - x', h) = \delta(x'). \tag{4}$$

– Remains monotonically decreasing throughout the entire domain.

– Has a compact support, meaning that for $|x - x'| > kh$

$$W(x - x', h) = 0. \tag{5}$$

– Is a symmetric function.

Initially, the kernel functions were defined such that each particle should have interactions with all others [7]. By introducing the concept of Neighboring particles[1], kernel function affect only a compact support around it were substituted (see Eq. (5)). Depending on the smoothing length parameter h, only a few number of particles in the entire space affect the approximated value of the kernel function (around 25 to 35 in 2D). In the current work, a cubic spline kernel function is used both for the balk fluid and the interface modeling while taking harmonic average.

$$W_{ij} = A \begin{cases} 2/3 - (r/h)^2 + 1/2(r/h)^3 & r/h \in [0,1) \\ 1/6(2 - r/h)^3 & r/h \in [1,2). \\ 0 & r/h \geq 2 \end{cases} \tag{6}$$

Hereafter, $W(x - x', h)$, will be shown by W_{ij} and $A = \frac{15}{7\pi h^2}$. Also, i, j, and r represent the index of the particle of interest, the index of its neighbors, and the smoothing radius.

To calculate the SPH gradients, one can show that it is sufficient to differentiate the kernel function $W(x - x', h)$. In other words, in SPH there is no need to differentiate the field function $f(x)$; instead one can differentiate the kernel function. The latter is one of the fascinating features of the SPH method which distinguishes this method from other mesh-based techniques. In this work, we use an improved version of the first derivative, presented in [34] as

$$\frac{\partial f_i^m}{\partial x_i^k} a_i^{kl} = \sum_j \frac{1}{\psi_j} (f_j^m - f_i^m) \frac{\partial W_{ij}}{\partial x_i^l}. \tag{7}$$

Also, the derivatives for vectorial and scalar quantities are calculated, respectively, as follows:

$$\frac{\partial^2 f_i^m}{\partial x_i^k \partial x_i^k} a_i^{ml} = 8 \sum_j \frac{1}{\psi_j} (f_i^m - f_j^m) \frac{\partial W_{ij}}{\partial x_i^l} \frac{r_{ij}^m}{r_{ij}^2}, \tag{8}$$

[1]particles that are located within the range of the kernel function with respect to the particle of interest. Outside of this range, the kernel function has already dropped to zero.

and

$$\frac{\partial^2 f_i}{\partial x_i^k \partial x_i^k}(2 + a_i^{kk}) = 8 \sum_j \frac{1}{\psi_j}(f_i - f_j) \frac{\partial W_{ij}}{\partial x_i^k} \frac{r_{ij}^k}{r_{ij}^2}, \tag{9}$$

where ψ is the particle number density and a_i^{kl} represents a corrective second rank tensor to avoid particle inconsistencies[9].

3. Governing Equations

Assuming an immiscible two-phase Newtonian, viscous, incompressible, isothermal fluid system, the corresponding mass and momentum conservations in a Lagrangian formulation are given as follows

$$\frac{D\rho}{Dt} = -\rho \nabla . \vec{V}, \tag{10}$$

and

$$\rho \frac{D\vec{V}}{Dt} = \nabla . \mathcal{T} + \vec{f}^b + \vec{f}^s + \vec{f}^e, \tag{11}$$

where, ρ is the fluid density, $\frac{D}{Dt}$ is the material time derivative operator[2], $\nabla . \vec{V}$ is the divergence of the velocity vector, $\mathcal{T}$ is the total stress tensor which is defined as $\mathcal{T} = -p\mathrm{I} + \tau$ where p is the static pressure, I is the identity matrix and $\tau = \mu(\nabla\vec{V} + (\nabla\vec{V})^T)$ is the viscous dissipation term for μ being the dynamic viscosity.
Additionally, $\vec{f}^b = \rho\vec{g}$ is the body force due to gravity and $\vec{f}^s$ is the surface tension which can be calculated using the volumetric force proposed by Brackbill [35], so called the Continuum Surface Force (CSF) method, as

$$\vec{f}^s = \gamma \kappa \vec{n} \delta^s. \tag{12}$$

Here, γ is the surface tension coefficient, $\kappa = -\nabla . \vec{n}$ is the interface curvature, $\vec{n} = \frac{\nabla C}{|\nabla C|}$ is the unit vector normal to the interface, and $\delta^s = |\nabla C|$ is surface Dirac-delta function, and finally, $\vec{f}^e$ is the electric field force.

To avoid sharp discontinuities at the interface, the smoothed color function of the particle i is defined as

$$C_i = \frac{\sum_j W_{ij} c_j}{\sum_j W_{ij}}, \tag{13}$$

where the color function c assigns a unit value to one phase and zero to the other phase in a two-phase system such that

[2] The material time derivative is a directional time derivative for a fixed point.

$$c_j = \begin{cases} 1, & \text{fluid A} \\ 0, & \text{fluid B} \end{cases}.$$

Furthermore, this approach provides a clear definition for the volume fraction of each fluid, i.e. $C_i^A = C_i$ and $C_i^B = 1 - C_i$ define the volume fraction corresponding to the fluid A and fluid B, respectively, such that $\sum_n C_i^n = 1$ for all n phases, here $n = 2$.

As mentioned before, in this study the electrostatics and the hydrodynamics are coupled together. This coupling is achieved through the Maxwell stress tensor. Maxwell equations provide a mathematical framework for the interaction and the connection between the electric and the magnetic fields [36]. Here, the EHD part of the system can be regarded as quasi-static model, and dynamic currents values are so low, hence the induced magnetic field effects are negligible. Therefore, the contribution from the induced magnetic field is neglected. Consequently, the volumetric electric force can be written as

$$\vec{f}^e = \nabla . T^E. \tag{14}$$

In case of an application of the external electric field on a multi-phase fluid flow, this new term for the electric force, will be added to the right hand side of the momentum equation (see Eq. (11)), where the Maxwell's stress tensor defines as

$$T^E = \vec{D}\vec{E} - \frac{1}{2}(\vec{D}.\vec{E})\mathrm{I}, \tag{15}$$

where $\vec{E}$ is an external electric field, $\vec{D} = \epsilon\vec{E}$ is the dielectric displacement vector, and ϵ is the electrical permittivity. Also, based on the Gauss's law [36]

$$\nabla . \vec{D} = q^v, \tag{16}$$

where q^v is the free electric charge density.

Application of Eqs. (15) and (14) will result in

$$\vec{f}^e = q^v\vec{E} - \frac{1}{2}\vec{E}.\vec{E}\nabla\epsilon. \tag{17}$$

In this work both fluids are considered to be leaky dielectric, (i.e. electric relaxation time is much shorter compared to its viscous counterpart or $t^e << t^v$).

4. Time integration

We apply a predictor-corrector scheme to advance the governing flow equations in time considering a first-order Euler approach. The time-step is selected based on Courant-Friedrichs-Lewy (CFL) condition in which $\Delta t = \mathrm{C_{CFL}} h/\mathrm{V}_{max}$, with V_{max} being the largest magnitude of particle velocity and the C_{CFL} is the constant taken as 0.25. During the predictor step, we first advance all the variables to an intermediate value denoted by (*), from the variables' value at the n-th time-step denoted by superscript (n), as

$$\vec{r}_i^* = \vec{r}_i^{(n)} + \vec{V}_i^{(n)} \Delta t + \delta \vec{r}_i^{(n)}, \tag{18}$$

$$\vec{V}_i^* = \vec{V}_i^{(n)} + \frac{RHS}{\rho_i^{(n)}} \Delta t, \tag{19}$$

$$\psi_i^{(*)} = \psi_i^{(n)} - \Delta t \psi_i^{(n)} (\nabla . \vec{V}_i^*). \tag{20}$$

RHS denotes the right hand side of Eq. (11), $\psi_i = \sum_j W_{ij}$, is the number density associated with the particle of interest i, which is calculated from the summation of kernel function at all neighboring particles j, δr_i is the artificial particle displacement, defined as $\delta r_i^k = \alpha \sum_j^N (r_{ij}^k / r_{ij}^3) r_{i,o}^2 V_{max} \Delta t$, and its constant α is set to 0.05 according to [34].

These intermediate values will then be used to solve the Poisson equation which gives the pressure value at the next time-step $(n+1)$. Using this pressure, new velocity and displacement vectors are updated as following

$$\nabla . \left(\frac{1}{\rho_i^*} \nabla p_i^{(n+1)} \right) = \frac{\nabla . \vec{V}_i^*}{\Delta t}, \tag{21}$$

$$\nabla . \vec{V}_i^{(n+1)} = \vec{V}_i^* - \frac{1}{\rho_i^*} \nabla p_i^{(n+1)} \Delta t, \tag{22}$$

$$\vec{r}_i^{(n+1)} = \vec{r}_i^{(n)} + 0.5 (\vec{V}_i^{(n)} + \vec{V}_i^{(n+1)}) \Delta t + \delta \vec{r}_i^{(n)}. \tag{23}$$

5. Results

5.1. Validation and convergence

To ensure a suitable particle resolution based on the numerically computed pressure jump across the interface, in Fig.2 the data is represented for 60×60, 100×100 and 140×140 grids. To study numerical convergence, a droplet with the radius of $r = 0.01$[m] is situated at the center of a square domain, $i.e.$ $x_o/r = y_o/r = 2$, with the side lengths of $x/r = y/r = 4$ (see Fig. 1). While the Dirichlet (no-slip) boundary condition is set for the velocity at all four boundaries, namely, *BC-X1, BC-X2, BC-Y1*, and *BC-Y2*, the Neumann boundary condition is applied for the pressure field. As for the hydrodynamics properties, we keep both viscosity and density ratios equal to unity such that $\rho_1 = \rho_2 = 1000$ [kg/m^3] and $\mu_1 = \mu_2 = 0.1$ [Pa.s] and set the surface tension to $\gamma = 0.01$ [N/m], given neither electrical nor gravitational force.

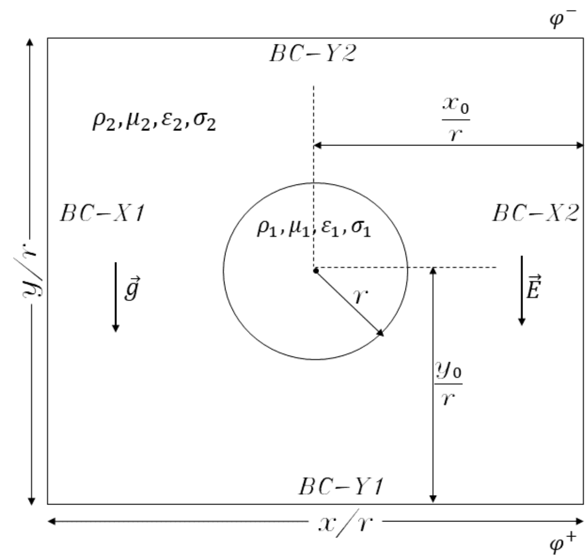

Figure (1) Schematic of the test case for validation and numerical convergence test, bubble rising as well as bubble deformation under the effect of electrohydrodynamics (EHD). For the first test case $\vec{g} = 0$ and $\vec{E} = 0$, for the second one $\vec{g} \neq 0$ and $\vec{E} = 0$ while for the third one $\vec{g} = 0$ and $\vec{E} \neq 0$

This problem, known as Young-Laplace problem, has an analytical solution which is $\Delta p = p_i - p_o = \gamma/r = 1$. As can be seen in Fig.2-Left, the pressure oscillations decrease by increasing the resolution from the coarser to the finest and the results, converging towards the analytical solution. It is noted that the relative error is less than 1% for the intermediate particle resolution. Therefore, we chose the 100×100 resolution for our simulations as it provides accurate results with reasonable computation cost. Similar simulations, with different surface tension coefficient are tested, while putting $r = 0.5[m]$ and keeping x/r and y/r ratios constant to validate the accuracy of the used method. As can be seen in Fig.2-Right, the pressure jump increases by an increment in the surface tension confirming the capability of the method to capture the physical jump across the interface. Once more for the reported simulations, the relative error is less than 1% when the numerical results are compared to the Laplace's law.

It is noteworthy to discuss the reason behind the different values obtained for the theoretical and numerical pressure jump at the interface. As mentioned before, the pressure and other flow field variables (velocity, color function, etc.) are approximated using the numerical smoothing scheme which converts the sharp values at the interface to smoother ones resulting in a loss of accuracy and introduction of spurious oscillations near the surface of the droplet. Furthermore, it is found that these spurious currents are generated because of an inappropriate evaluation of the curvature of the circular droplet due to unreliable values for the unit normal vector ($\vec{n} = \frac{\nabla C}{|\nabla C|}$) in the surface tension force calculation [37].

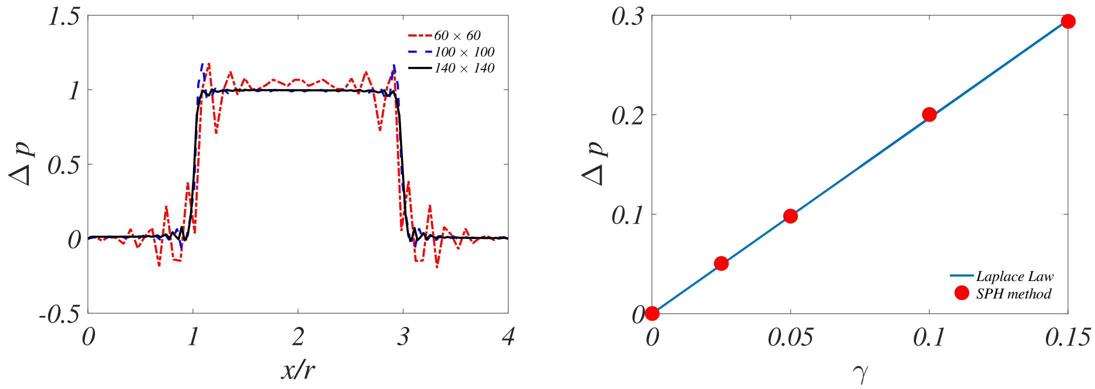

Figure (2) Comparison of (left) the pressure jump across the droplet interface for three particle resolutions and (right) its comparison with the theoretical pressure jump, *i.e.* Laplace's law, for different cases.

5.2. *Bubble rising*

In this section, the ISPH method is applied to test and to validate the simulation of the bubble rising problem due to the gravitational force. The computational geometry for this test case is similar to the one shown in Fig. 1 except that the domain size is increased in the normal direction (orthogonal), *i.e.* $x/r = 6$ and $y/r = 12$, and the bubble is initially placed such that $x_o/r = 3$ and $y_o/r = 2.4$. The grid resolution is set to 240×480 in x and y direction, respectively. The velocity boundary conditions are set to be free slip for $BC - X1$ and $BC - X2$, and no slip for $BC - Y1$ and $BC - Y2$. Also, pressure boundary conditions are set to be Dirichlet with a constant value at $BC - Y2$ and Neumann for the other three boundaries ($\nabla p \cdot \vec{n} = 0$) where $\vec{n}$ is normal direction to the given boundary.

Here, both bubble and bulk phases are set to have stationary conditions at initial time step. The bubble starts to rise during the simulation due to the gravitational forces. This problem can be characterized by Reynolds and Bond numbers defined as following:

$$Re = \frac{\rho_2 g^{0.5} (2r_o)^{1.5}}{\mu_2}, \tag{24}$$

and

$$Bo = \frac{\rho_2 g (2r_o)^2}{\gamma}. \tag{25}$$

respectively.

For the first simulation, a case with low density and viscosity ratios and high surface tension is considered, where $\rho_2/\rho_1 = 10$ with $\rho_1 = 100$ [kg/m3], $\mu_2/\mu_1 = 10$ with $\mu_1 = 1$[Pa.s], and surface tension coefficient is $\gamma = 24.5$[N/m]. Additionally, the gravity is set to be $\vec{g} =$

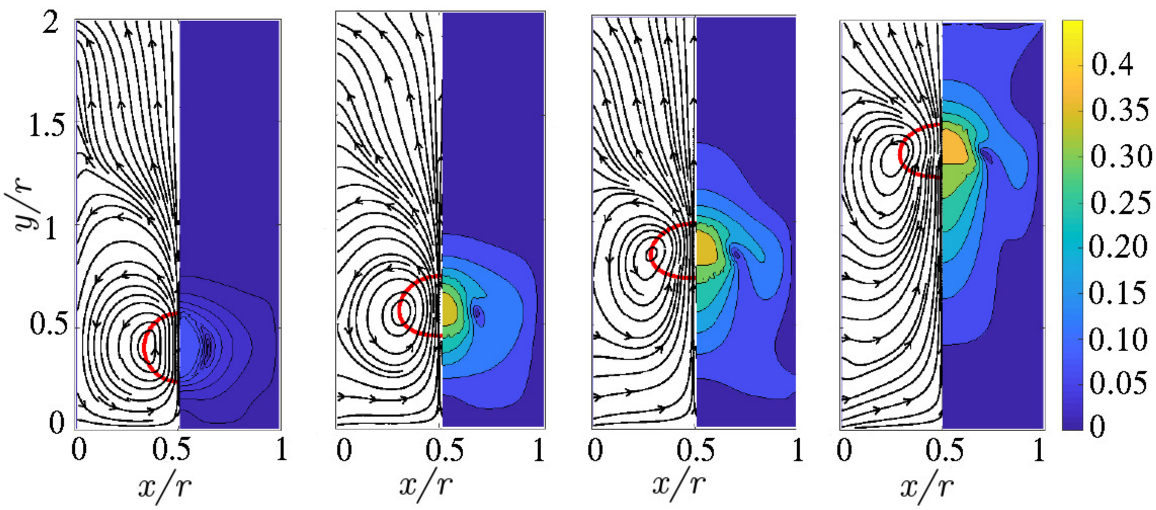

Figure (3) Time evolution of bubble rising problem with the density ratio of $\rho_1/\rho_2 = 0.1$ and viscosity ratio of $\mu_1/\mu_2 = 0.1$ at different dimensionless times $t^* = 0.5$, $t^* = 18.5$, $t^* = 37$ and $t^* = 64.8$. Here the dimensionless time is defined as $t^* = t\sqrt{(g/D)}$ and Reynolds and Bond numbers are $Re = 35$ and $Bo = 10$, respectively. The left half of each snapshot shows the velocity streamlines in black and the droplet interface in red, while the right half shows the velocity magnitude's 10 highest levels' contour in the range of $[0, 4.5]$ [m/s].

-1[m/s2] in y direction such that it produces Reynolds number $Re = 35$, and the Bond number $Bo = 10$ for this case. The time snapshot of this test case for dimensionless times of $t^* = 0.5$, $t^* = 18.5$, $t^* = 37$ and $t^* = 64.8$ are shown in Fig. 3. As observed in this figure, the bubble starts to rise straight upwards due to the gravity, while its velocity increases from zero to 0.36 [m/s] and remains constant until it feels the pressure coming from the stationary upper-wall. Additionally, the bubble shape is changing from circular shape to a quasi elliptical one due to hydrodynamic pressures on its tip. The final shape comes from the competition among surface tension, gravitational, and viscous forces. As it is observed, the shape remains unchanged after some time steps which is the main reason for the bubble's almost constant terminal velocity.

Fig. 4 shows the mean migration velocity and the position of the droplet with respect to dimensionless time $t^* = t\sqrt{(g/D)}$, which are in agreement with the results of [31] and [38]. Here, the velocity gradient near the stationary wall starts to deviates at the final times which could be due to the confinement effects.

To show the applicability of the proposed algorithm for capturing larger deformations and breakups, we perform a second bubble rising test case. This time, the computational domain size is $x/r = 6$ and $y/r = 10$ with the particle resolution of 240×400. The bubble is initially placed at $x_o/r = 3$ and $y_o/r = 2$. Here, all four boundaries have no slip boundary condition for

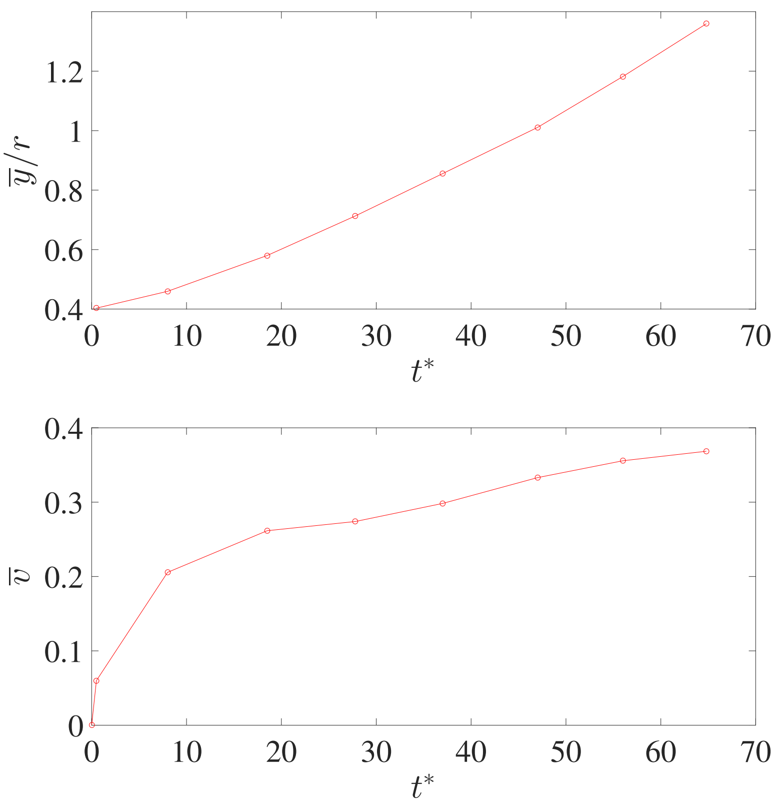

Figure (4) The average normalized central position of the droplet, $\bar{y}$ (top) and its average vertical migration velocity, $\bar{v}$ (bottom) as a function of dimensionless time, t^*.

velocity. However, the pressure boundary conditions are kept the same as before. The gravity is selected as $\vec{g} = -1[\text{m/s2}]$ in y direction, while the surface tension coefficient is set to be $\gamma = 20$ [N/m]. Additionally, the density and viscosity ratios are $\rho_2/\rho_1 = 1000$ and $\mu_2/\mu_1 = 2.828/10$ with $\rho_1 = 1$ [kg/m3] and $\mu_1 = 1$[Pa.s], respectively. These choices are for mimicking the test case presented in [15] in order to produce the fluid flow system with Reynolds and Bond numbers of $\boldsymbol{Re} = 1000$ and $\boldsymbol{Bo} = 200$, respectively.

The snapshots of our current simulations are illustrated (middle) in Fig. 5 for the dimensionless times between $t^* = 3.2$ and $t^* = 5.6$ with a time increment of $\Delta t^* = 0.4$. These snapshots are compared to their experimental (top) and Volume of Fluid method (bottom) counterparts, presented in [39] and [40], respectively. As can be seen, the proposed ISPH approach can predict the large deformation and bubble breakup as accurate as its well establish mesh based method. The presented Volume of fluid (VoF) method uses a hybrid VoF-level-set method [40] to accurately capture the interface.

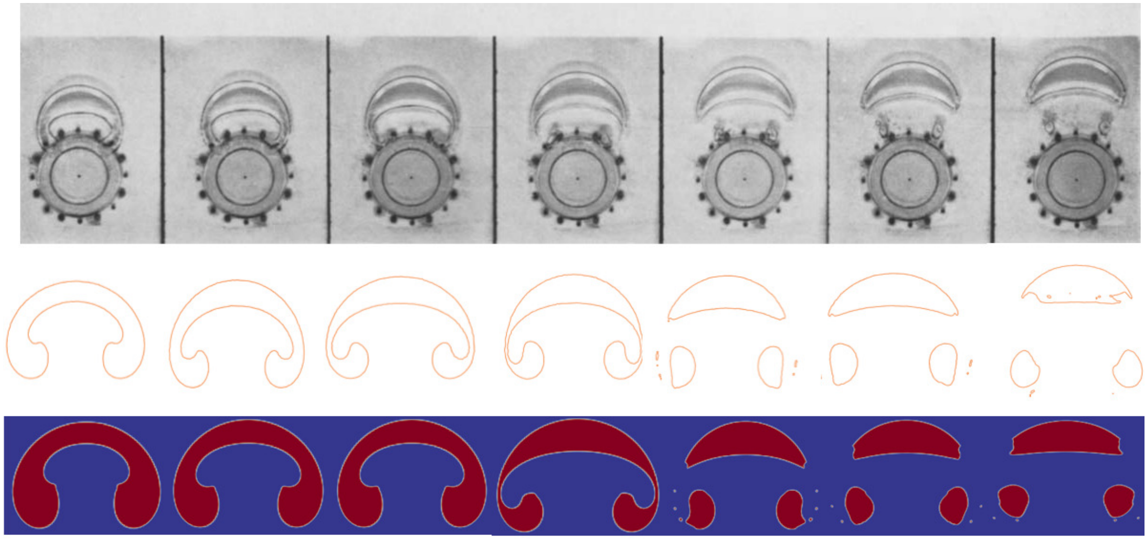

Figure (5) Comparison of bubble rising and break up due to gravitational and hydrodynamic forces using experiment [39], SPH method and Volume of Fluid method [40], respectively from top to bottom rows. Here, the density ratio $\rho_2/\rho_1 = 1000$ and viscosity ratio $\mu_2/\mu_1 = 10$ are applied. Reynolds and Bond numbers, as previously defined, are $Re = 1000$ and $Bo = 200$, respectively. The dimensionless time is defined as $t^* = t\sqrt{g/r_o}$, starting from $t^* = 3.2$ at the very fist frame on the left, up to $t^* = 5.6$, with a time increment of 0.4 per frame.

5.3. *EHD droplet deformation*

In this section, we consider a suspended circular droplet under the effect of an external applied electric field. The schematic of the computational domain is similar to what is presented in Fig. 1 with an increment in the size of the domain. Here, we double the domain size in each direction, $i.e.$ $x/r = 8$ and $y/r = 8$, in order to reduce the confinement effect. In Fig. 6-left, a particle resolution of 240×240 is used with a circular droplet initially placed at the center of computational domain. The initial zero velocity are assigned to both fluids and wall particles. Density ratio and viscosity ratio are set to unity with values of $\rho_1 = \rho_2 = 1000$ [kg/m^3] and $\mu_1 = \mu_2 = 1$[Pa.s]. The surface tension coefficient $\gamma = 1$[N/m]. The velocity and pressure boundary conditions are exactly the same as those imposed in section 5.1. The electrical boundary conditions are Dirichlet ($\varphi = cte.$) and Neumann boundary ($\nabla\varphi \cdot \vec{n} = 0$) conditions for horizontal ($i.e.$ $BC - Y1$ and $BC - Y2$) and vertical walls ($i.e.$ $BC - X1$ and $BC - X2$), respectively, where $\vec{n}$ is normal direction to the given boundary.

The deformation of a suspended circular droplet under such conditions is a commonly utilized test case for validation of a EHD solver, where two theories are available in the literature. Taylor [41] estimates the droplet deformation D_T as

$$D_T = \frac{9 f_{dT} E_o^2 \epsilon_2 r_o}{8(2+R)^2\gamma}, \tag{26}$$

where f_{dT} is the discriminating function evaluated as

$$f_{dT} = R^2 + 1 - 3.5S + 1.5R. \tag{27}$$

For the same problem, Feng [42] suggests the following relation

$$D_F = \frac{f_{dF} E_o^2 \epsilon_1 r_o}{3(1+R)^2 S\gamma}, \tag{28}$$

where f_{dF} is estimated from

$$f_{dF} = R^2 + 1 - 3S + R. \tag{29}$$

In Eqs. (26) and (28), r_o is the initial droplet radius before its deformation and E_o is the electric field intensity in vertical direction which is calculated from $E_o = (\varphi^+ - \varphi^-)/H$, H being the domain height. Additionally, the permittivity ratio and the conductivity ratio of droplet to the balk are called S and R, presented as

$$S = \frac{\epsilon_1}{\epsilon_2}, \quad R = \frac{\sigma_1}{\sigma_2}, \tag{30}$$

where ϵ and σ are the electrical permittivity and conductivity, respectively. Also the subscripts 1 and 2 show, droplet and bulk medium properties, respectively.

Another point in the theory of droplet deformation is to investigate the velocity recirculation vectors inside and outside of the droplet when a vertical electric field is applied. The relative differences in the electric permittivity and conductivity of both constituent phases define the direction of the flow rotation in either phase. This is shown for two cases in Fig. 6. On the left side test case is adopted for $S = 0.5$ and $R = 0.05$ with the electrical permittivity of the droplet (ϵ_1) being 0.5 [F/m] which is half of that of the bulk fluid. Also, the electrical conductivity of the droplet (σ_1) is set to 150 [S/m] which is three-times more than the background fluid. On the right side of Fig. 6, the test case has $S = 0.5$ and $R = 3$ with $\epsilon_1 = 0.5$ and $\sigma_1 = 1$. As can be seen in the left sub-figure, the re-circulation zone in the first quarter (i.e. the top-right quarter inside the droplet) of the droplet orients clockwise. This should be the case for $S > R$ and is consistent with the results of [29]. The opposite flow circulation pattern should be expected for the case of $S < R$ as it also presented on the right side of the same figure.

Additionally, Eqs. (27) and (29) define the sign of Eqs. (26) and (28), respectively. The positive sign, so called prolate deformation, indicates that the droplet is elongated in the direction parallel to the electric field. The positive sign, so called oblate deformation, shows the droplet elongation in the opposite direction. For the comparison with the simulation results, we define the numerical deformation as

$$D_N = \frac{A - B}{A + B}, \tag{31}$$

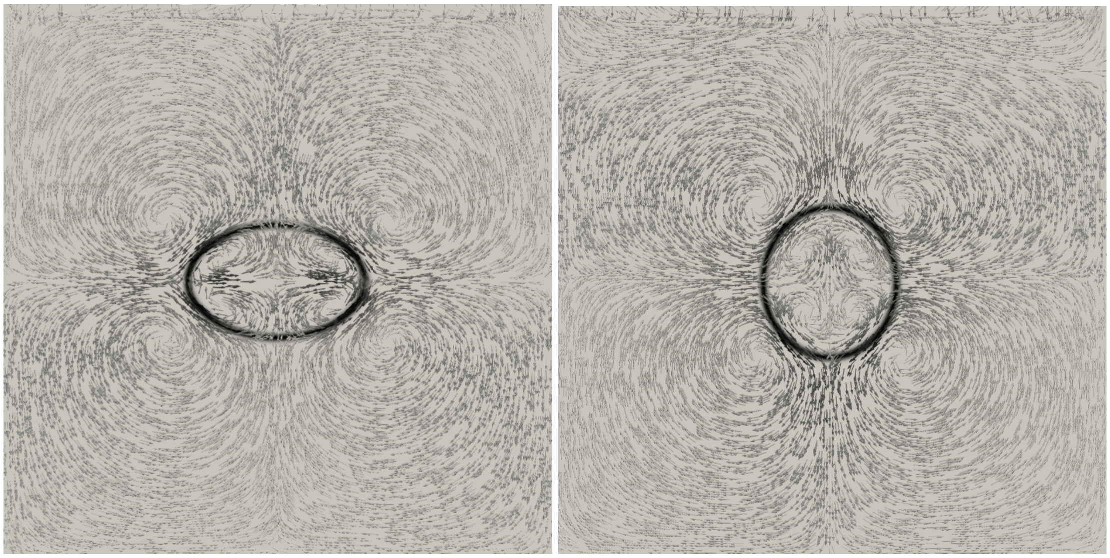

Figure (6) Deformation of a suspended droplet in response to an external vertical electric field in the steady-state simulation for the cases with (left) $S = 0.5$, $R = 0.05$ and (right) $S = 0.5$, $R = 3$.

where A and B are the elliptic droplet diameters, parallel and perpendicular to the direction of the external electric field, respectively, at the steady state condition. When this parameter is equal to zero, the droplet keeps its initial circular shape. On the other hand, more deviation from zero indicates more deformation from its initial shape.

Fig. 7 provides comparison between the current ISPH results and the two aforementioned theories for multiple cases. As can be seen, numerical data reasonably follow the available theories. However, in most of the cases, an over-prediction is reported by the simulations. Some might be some possible reasons for such behaviour can be mentioned: (i) in the theory it is assumed that the droplet remains circular even after applying the electric field. This means the change in the curvature is not integrated in the deformation equation, but only the surface tension coefficient. (ii) Another reason might be due to the confinement effect. In theories, it is assumed that the droplet is suspended in an unbounded domain for simplicity. However, providing such domain numerically, or even with twice larger computational domain, is very expensive computationally. Finally, the hydrodynamical properties of droplets such as density and viscosity are not taken into account theoretically and the problem is considered to be inviscid.

5.4. Couette Flow

This section investigates the deformation of a droplet suspended between two parallel plates subjected to a constant shear. The flow configuration, known as Couette flow, is presented in Fig. 8. In this case, the flow is driven by viscous forces or pressure gradients [43]. Different cases

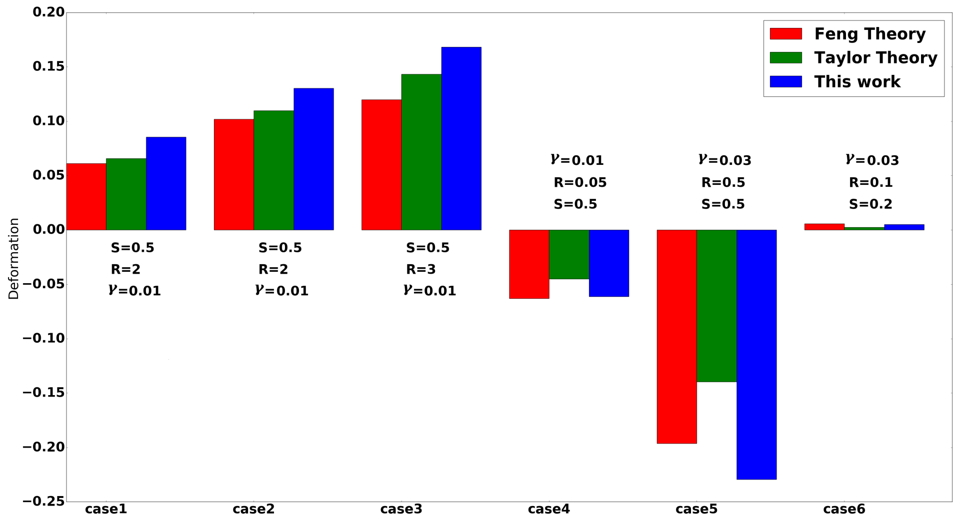

Figure (7) Comparison of deformation for all cases. permittivity ratio, conductivity ratio and surface tension coefficient of each simulation, S, R, γ, respectively, mentioned below or above the corresponding case.

with and without an external electric field with the magnitude of unity perpendicular to the flow direction are simulated.

The computational domain consists of a rectangle box with the size of $x/r = 16$ and $y/r = 4$ discretized by a set of initially equally spaced $400{\times}100$ particles, arranged in a Cartesian grid. The two-phase system contains a droplet with the initial radius of r_o, placed in the middle of the domain, and the balk fluid with the same density of $\rho_1 = \rho_2 = 1000$ [kg/m^3] and the dynamic viscosity of $\mu_1 = \mu_2 = 0.2$ [Pa.s]. The velocity boundary conditions are set to Dirichlet (no-slip) on the plates ($i.e.$ $BC-Y1$ and $BC-Y2$) and periodic for the inlet and outlets ($i.e.$ $BC-X1$ and $BC-X2$). The pressure boundary conditions is Dirichlet $BC-Y2$ and Neumann for the rest of boundaries. Also, the boundary conditions for electrical potential are of Dirichlet at the walls ($i.e.$ $\varphi = cte$ in $BC-Y1$ and $BC-Y2$) and periodic for the two other sides ($i.e.$ $BC-X1$ and $BC-X2$).

Initially, the upper and the lower wall velocities are set to $U_o/2$ and $-U_o/2$, respectively, where $U_o = 0.02$ [m/s]. Additionally, particles inside the droplet are initialized to be at rest, while background fluid particles having undisturbed Couette flow velocity. The simulations are performed for a range of electrical permittivity and electrical conductivity ratios shown as (S, R), while neglecting the gravity and keeping the surface tension coefficient constant $\gamma = 0.02$ [N/m]. The droplet radius is a quarter of the distance between two parallel plates (i.e. $r = H/4$). The dimensionless Reynolds, Weber and Electroinertial numbers, respectively, are

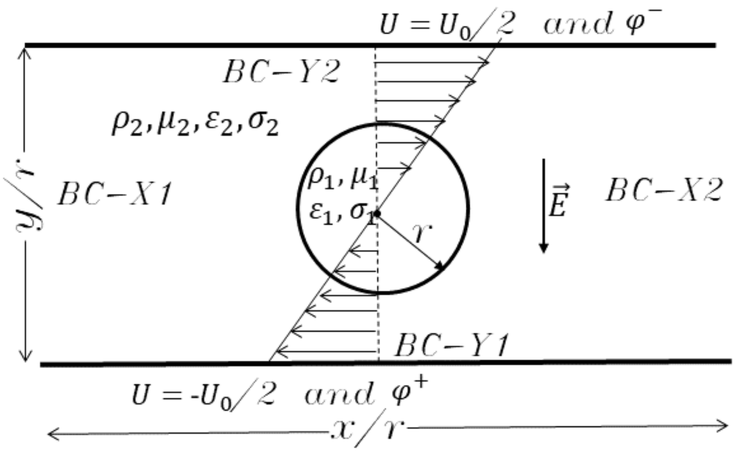

Figure (8) Schematic of the Couette flow test case.

as follows

$$Re = \frac{\rho_2 U_o r_o}{\mu_2}, \qquad We = \frac{\rho_2 U_o^2 r_o}{\gamma}, \qquad Ei = \frac{\rho_2 U_o^2}{\epsilon_2 E_o^2}, \tag{32}$$

where $Re = 1$, $We = 0.2$, and $Ei = 50$.

Fig.9 shows the time evolution of the droplets' deformation under the same external electric field and the shear stress conditions, but for different working fluids having different electrical permittivity and conductivity ratios ($i.e.$ only a change in S and R is considered here). In this figure, the dimensionless time is defined as $t^* = tU_o/r_o$, while the droplet deformation is calculated from

$$D_f = \frac{L_{max} - L_{min}}{L_{max} + L_{min}}, \tag{33}$$

where L_{max} and L_{min} are major and minor droplet diameters, respectively. As can be seen in this figure, the droplet deformation increases when an external electric field is applied regardless of S and R. Additionally, at the constant electrical permittivity ratio, larger deformations can be achieved by an increment in the electrical conductivity ratio when $S > R$. However, for the similar condition ($i.e.$ $S = cte.$), smaller deformations are seen by an increment in the electrical conductivity ratio when $S < R$. Similarly, at constant electrical conductivity ratio larger electrical permitivities result in larger droplet deformations for $R < S$, while decreases the same for $S < R$. It is noted that the (5.0, 0.2) and (5.0, 0.5) test problems did not reach a steady profile during the simulation time, here fixed at $t^* = 1$ due to large computational costs. Fig. 10 provides a comparison on the interface shape in the absence (in blue) and the presence of the electric field (in black) at this time. Following the previous figure, it can be seen that the droplets are more slender for larger deformation factors.

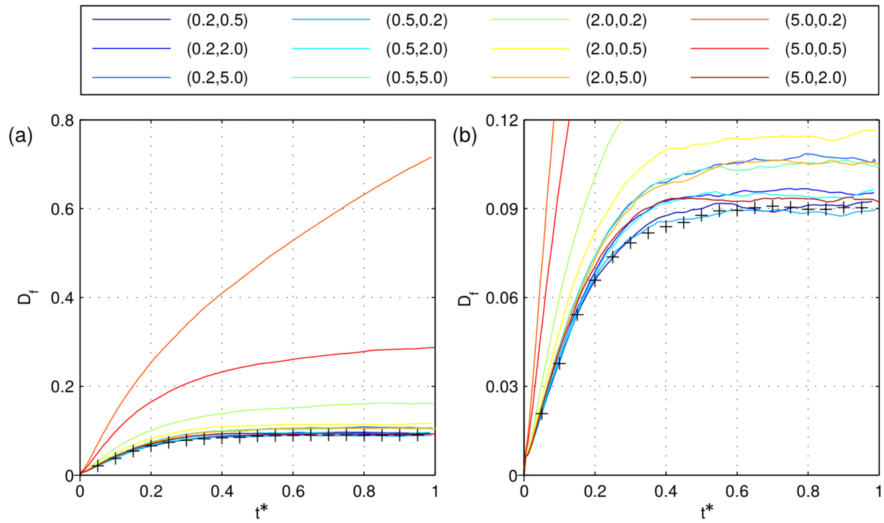

Figure (9) Numerical deformation for twelve cases (Left), a close-up look at the rate of deformation at the steady state (Right). Cases without electric field are denoted by a black + sign. The pair number on the legend box, corresponds to the electrical permittivity and electrical conductivity (S, R), respectively.

It is notable that the angle between the major axis of the elliptic droplet and the stream-wise direction become smaller with an increment in the conductivity ratio, while the cases of (5.0, 0.2) and (5.0, 0.5) are immediately distinguishable due to their larger deformations. This elongation is due to the suppression of surface tension forces which is the result of the larger electric field force at higher electrical conductivity ratios. It is also noted that the droplet is no longer elliptical and is suspected to have the breakup at larger time steps.

Finally, the time snapshot of an extreme test case with the electrical permittivity ratio of $S = 10$ and the electrical conductivity ratio of $R = 0.2$ is illustrated in Fig. 11 to show the ability of the presented method to capture very large deformations with the interfacial topological change. Here, the interface is represented by red color, while the velocity streamlines and electrical vectors are represented by blue and black arrows, respectively. In this case, the circular droplet becomes elliptical soon after the start of the simulation. The elliptical interface is elongated in the stream-wise axis direction due to the four re-circulation zones in the bulk flow just next to the interface. Soon after that, pairs of re-circulation merge with each other at the both tips of the droplet and cause the creation of the third re-circulation in its center. By time, the droplet gets folded in four different places and new re-circulation zones appear close to the interface which makes the droplet very susceptible to breakup. As can be seen, this is a promising test problem to show the ability of the present ISPH code to treat the complex multi-phase fluid behavior under an extreme EHD conditions with large interfacial deformation.

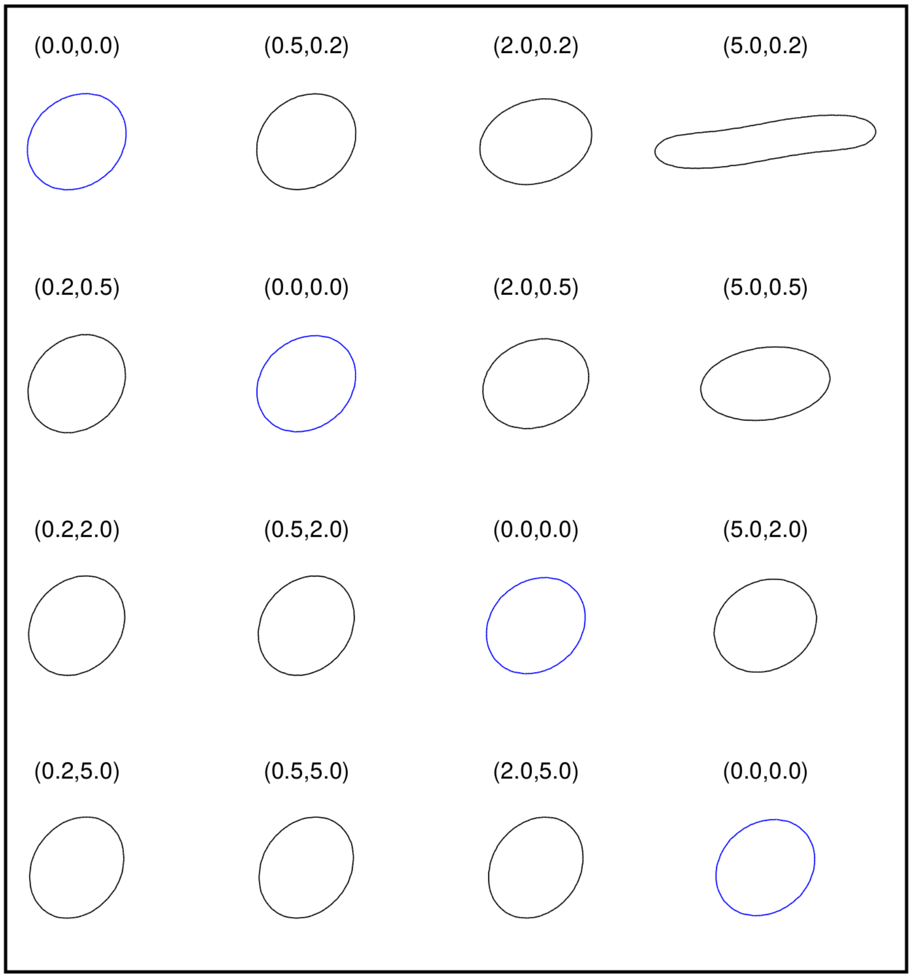

Figure (10) Bubble interface at $t^* = 1$. The pair number above each case corresponds to the electrical permittivity and electrical conductivity (S, R), respectively. If zero, the electric field is not applied.

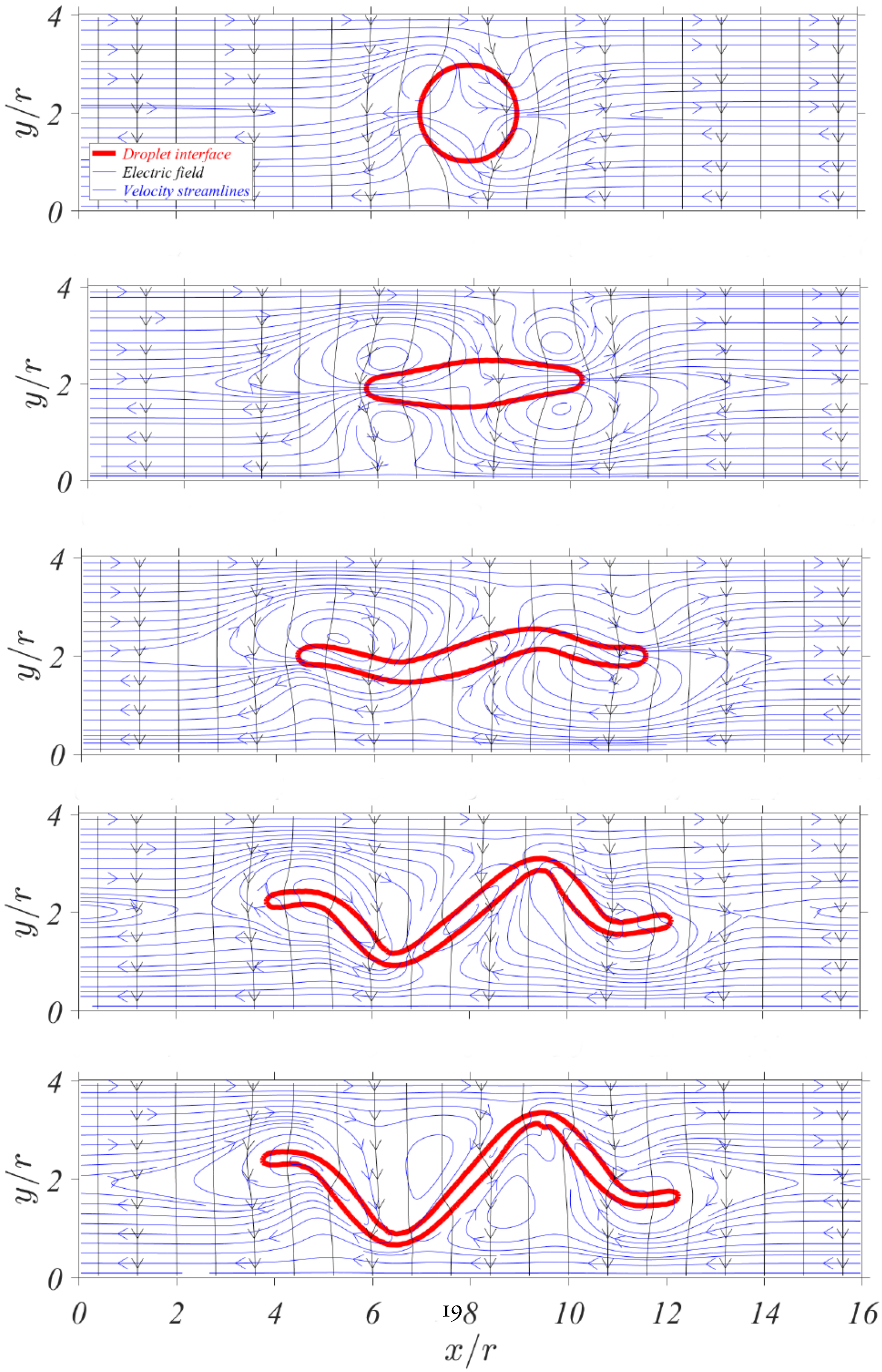

Figure (11) Deformation of a suspended droplet in Couette flow with $S = 10$ and $R = 0.2$ subject to electric field at $t^* = 0$, $t^* = 0.4$, $t^* = 0.8$, $t^* = 1.2$ and $t^* = 1.6$, respectively, from top to bottom where dimensionless time is defined by $t^* = tU_o/r$. The velocity streamlines (in blue), the electric field vectors (in black) and the droplet interface (in red) are shown at five moments.

6. Summary

In this work, we presented an effective multi-phase Incompressible Smoothed Particle Hydrodynamics (ISPH) approach to simulate complex multi-physics electrohydrodynamics (EHD) problems. We showed a step-by-step validation of the multiphase code for surface tensions, hydrodynamic forces and electric forces, respectively, by solving Laplace's law, bubble rising and buoyant droplet deformation under an applied electric field problems. Results are validated either against available analytical or numerical results. An overall satisfactory agreement were found. Finally, we presented, for the first time, results of droplet deformation under sheared Couette flow with external electric field for a range of simulation parameters. Different parameters such as time resolved topological changes, droplet deformation magnitudes as well as velocity field and electrical potential vectors were presented and compared with each other. It was shown that the current ISPH approach is able to be easily adopted for different multi-physics problems. It is also capable of predicting large interfacial topological changes such as folding and breakup. In future, our strategy would be to include more complex transport and multi-physics phenomena.

Acknowledgment

This work has benefited from the financial support of TOTAL SA within the framework of a call for projects with exploratory projects coordinated by TOTAL SA and the CNRS. The authors also acknowledge the access to French HPC resources provided by the French regional computing center of Normandy CRIANN (2017002). The first author acknowledges the financial supports provided by Normandy region. The second author acknowledge the support provided by Alexander von Humboldt Foundation through the project FRA-1204799-HFST-E for the experienced researcher.

References

[1] Q. Xiong, S.-C. Kong, High-resolution particle-scale simulation of biomass pyrolysis, ACS Sustainable Chemistry & Engineering 4 (2016) 5456–5461.

[2] M. Sarafraz, M. S. Shadloo, Z. Tian, I. Tlili, T. A. Alkanhal, M. R. Safaei, M. Goodarzi, M. Arjomandi, Convective bubbly flow of water in an annular pipe: Role of total dissolved solids on heat transfer characteristics and bubble formation, Water 11 (2019) 1566.

[3] A. Izadi, M. Siavashi, Q. Xiong, Impingement jet hydrogen, air and cuh2o nanofluid cooling of a hot surface covered by porous media with non-uniform input jet velocity, International Journal of Hydrogen Energy 44 (2019) 15933–15948.

[4] M. V. Bozorg, M. H. Doranehgard, K. Hong, Q. Xiong, Cfd study of heat transfer and fluid flow in a parabolic trough solar receiver with internal annular porous structure and synthetic oil–al2o3 nanofluid, Renewable Energy 145 (2020) 2598–2614.

[5] M. Y. A. Jamalabadi, M. DaqiqShirazi, A. Kosar, M. S. Shadloo, Effect of injection angle, density ratio, and viscosity on droplet formation in a microfluidic t-junction, Theoretical and Applied Mechanics Letters 7 (2017) 243–251.

[6] R. Sadeghi, M. S. Shadloo, M. Hopp-Hirschler, A. Hadjadj, U. Nieken, Three-dimensional lattice boltzmann simulations of high density ratio two-phase flows in porous media, Computers & Mathematics with Applications 75 (2018) 2445–2465.

[7] R. A. Gingold, J. J. Monaghan, Smoothed particle hydrodynamics: theory and application to non-spherical stars, Monthly notices of the royal astronomical society 181 (1977) 375–389.

[8] L. B. Lucy, A numerical approach to the testing of the fission hypothesis, The astronomical journal 82 (1977) 1013–1024.

[9] M. S. Shadloo, A. Zainali, S. H. Sadek, M. Yildiz, Improved incompressible smoothed particle hydrodynamics method for simulating flow around bluff bodies, Computer methods in applied mechanics and engineering 200 (2011) 1008–1020.

[10] M. S. Shadloo, A. Zainali, M. Yildiz, A. Suleman, A robust weakly compressible sph method and its comparison with an incompressible sph, International Journal for Numerical Methods in Engineering 89 (2012) 939–956.

[11] M. Hirschler, P. Kunz, M. Huber, F. Hahn, U. Nieken, Open boundary conditions for isph and their application to micro-flow, Journal of Computational Physics 307 (2016) 614–633.

[12] S. Marrone, M. Antuono, A. Colagrossi, G. Colicchio, D. Le Touzé, G. Graziani, δ-sph model for simulating violent impact flows, Computer Methods in Applied Mechanics and Engineering 200 (2011) 1526–1542.

[13] M. S. Shadloo, R. Weiss, M. Yildiz, R. A. Dalrymple, et al., Numerical simulation of long wave runup for breaking and nonbreaking waves, International Journal of Offshore and Polar Engineering 25 (2015) 1–7.

[14] H. Gotoh, A. Khayyer, On the state-of-the-art of particle methods for coastal and ocean engineering, Coastal Engineering Journal 60 (2018) 79–103.

[15] A. Zainali, N. Tofighi, M. S. Shadloo, M. Yildiz, Numerical investigation of newtonian and non-newtonian multiphase flows using isph method, Computer Methods in Applied Mechanics and Engineering 254 (2013) 99–113.

[16] N. Grenier, M. Antuono, A. Colagrossi, D. Le Touzé, B. Alessandrini, An hamiltonian interface sph formulation for multi-fluid and free surface flows, Journal of Computational Physics 228 (2009) 8380–8393.

[17] M. S. Shadloo, M. Yildiz, Numerical modeling of kelvin–helmholtz instability using smoothed particle hydrodynamics, International Journal for Numerical Methods in Engineering 87 (2011) 988–1006.

[18] C. Ulrich, M. Leonardi, T. Rung, Multi-physics sph simulation of complex marine-engineering hydrodynamic problems, Ocean Engineering 64 (2013) 109–121.

[19] M. Hopp-Hirschler, M. S. Shadloo, U. Nieken, Viscous fingering phenomena in the early stage of polymer membrane formation, Journal of Fluid Mechanics 864 (2019) 97–140.

[20] M. Hopp-Hirschler, M. S. Shadloo, U. Nieken, A smoothed particle hydrodynamics approach for thermo-capillary flows, Computers & Fluids 176 (2018) 1–19.

[21] M. Shadloo, G. Oger, D. Le Touzé, Smoothed particle hydrodynamics method for fluid flows, towards industrial applications: Motivations, current state, and challenges, Computers & Fluids 136 (2016) 11–34.

[22] M. Rezavand, M. Taeibi-Rahni, W. Rauch, An isph scheme for numerical simulation of multiphase flows with complex interfaces and high density ratios, Computers and Mathematics with Applications 75 (2018) 2658 – 2677.

[23] Y. Hu, D. Li, X. Niu, Y. Zhang, Lattice boltzmann model for the axisymmetric electro-thermo-convection, Computers and Mathematics with Applications 78 (2019) 55 – 65.

[24] J. Weirather, V. Rozov, M. Wille, P. Schuler, C. Seidel, N. A. Adams, M. F. Zaeh, A smoothed particle hydrodynamics model for laser beam melting of ni-based alloy 718, Computers and Mathematics with Applications (2018).

[25] K. Abdella, H. Rasmussen, I. Inculet, Interfacial deformation of liquid drops by electric fields at zero gravity, Computers and Mathematics with Applications 31 (1996) 67 – 82.

[26] X. Huang, L. He, X. Luo, H. Yin, D. Yang, Deformation and coalescence of water droplets in viscous fluid under a direct current electric field, International Journal of Multiphase Flow 118 (2019) 1 – 9.

[27] Q. Yang, B. Q. Li, Y. Ding, 3d phase field modeling of electrohydrodynamic multiphase flows, International Journal of Multiphase Flow 57 (2013) 1 – 9.

[28] F. Alberini, D. Dapelo, R. Enjalbert, Y. V. Crombrugge, M. J. Simmons, Influence of dc electric field upon the production of oil-in-water-in-oil double emulsions in upwards mm-scale channels at low electric field strength, Experimental Thermal and Fluid Science 81 (2017) 265 – 276.

[29] M. Shadloo, A. Rahmat, M. Yildiz, A smoothed particle hydrodynamics study on the electrohydrodynamic deformation of a droplet suspended in a neutrally buoyant newtonian fluid, Computational Mechanics 52 (2013) 693–707.

[30] A. Rahmat, M. Yildiz, A multiphase isph method for simulation of droplet coalescence and electro-coalescence, International Journal of Multiphase Flow 105 (2018) 32–44.

[31] A. Rahmat, N. Tofighi, M. Yildiz, Numerical simulation of the electrohydrodynamic effects on bubble rising using the sph method, International Journal of Heat and Fluid Flow 62 (2016) 313 – 323.

[32] A. Rahmat, N. Tofighi, M. Shadloo, M. Yildiz, Numerical simulation of wall bounded and electrically excited rayleigh–taylor instability using incompressible smoothed particle hydrodynamics, Colloids and Surfaces A: Physicochemical and Engineering Aspects 460 (2014) 60–70.

[33] M. Liu, G. Liu, K. Lam, Constructing smoothing functions in smoothed particle hydrodynamics with applications, Journal of Computational and Applied Mathematics 155 (2003) 263 – 284.

[34] M. Shadloo, A. Zainali, M. Yildiz, Simulation of single mode rayleigh–taylor instability by sph method, Computational Mechanics 51 (2013) 699–715.

[35] J. Brackbill, D. Kothe, Z. CA, A continuum method for modeling surface tension, Journal of Computational Physics (1992) 335–354.

[36] D. Fleisch, A guide to maxwell equations, Cambridge University Press (2008).

[37] M. Sussman, E. G. Puckett, A Coupled Level Set and Volume-of-Fluid Method for Computing 3D and Axisymmetric Incompressible Two-Phase Flows, Journal of Computational Physics 162 (2000) 301–337.

[38] A. Zhang, Z. Guo, Q. Wang, S. Xiong, Three-dimensional numerical simulation of bubble rising in viscous liquids: A conservative phase-field lattice-boltzmann study, Physics of Fluids 31 (2019) 063106.

[39] J. K. Walters, J. F. Davidson, The initial motion of a gas bubble formed in an inviscid liquid, Journal of Fluid Mechanics 17 (1963).

[40] A. Asuri Mukundan, T. Ménard, A. Berlemont, J. C. C. Brändle De Motta, R. Eggels, Validation and Analysis of 3D DNS of planar pre-filming airblast atomization simulations, in: In Proceedings of ILASS Americas, 30th Annual Conference on Liquid Atomization and Spray Systems. May 12th-15th, Tempe, Arizona, USA, Tempe, United States.

[41] G. I. Taylor, A. D. McEwan, L. N. J. de Jong, Studies in electrohydrodynamics. i. the circulation produced in a drop by an electric field, Proceedings of the Royal Society of London. Series A. Mathematical and Physical Sciences 291 (1966) 159–166.

[42] J. Q. Feng, Electrohydrodynamic behaviour of a drop subjected to a steady uniform electric field at finite electric reynolds number, Proceedings of the Royal Society of London. Series A: Mathematical, Physical and Engineering Sciences 455 (1999) 2245–2269.

[43] Deformation of a droplet in Couette flow subject to an external electric field simulated using ISPH, PARTICLES, Barcelona, Spain, 2015.